Experiments and reduced order modeling of symmetry breaking in Rayleigh-Taylor mixing

Mohammadjavad Mohammadi, Mohammad Khalifi, Nasser Sabet, and Hassan Hassanzadeh*

Department of Chemical & Petroleum Engineering, Schulich School of Engineering, University of Calgary, Calgary, Alberta, Canada T2N 1N4

(Received 26 April 2023; accepted 4 October 2023; published 30 October 2023)

We report experiments of fingering asymmetry in Rayleigh-Taylor (RT) mixing at an extremely large viscosity ratio ($M \approx 5 \times 10^5$) and Rayleigh numbers [Ra $\sim 10^5$–(3×10^6)]. Our experiments confirm the asymmetric growth of RT instabilities across an upward-moving interface with strong downward fingering. As the Ra increases, the downward fingers reach the bottom boundary faster, resulting in a lower dispersion at the early time. However, this dynamic is not persistent since the system undergoes vigorous mixing after the elongated fingers reach the bottom boundary. A one-dimensional dispersion model is developed to simulate the RT mixing, which predicts the upward-moving front and mixing across the interface.

DOI: 10.1103/PhysRevFluids.8.103504

I. INTRODUCTION

When a heavier fluid lies on top of a lighter one, the density difference between the two fluids leads to a buoyancy-driven mixing known as the Rayleigh-Taylor (RT) instability [1]. In addition, the two fluids often have different viscosities and are partially or fully miscible, resulting in a concentration dependency of the mixture density and viscosity. Hence, the interplay of density and viscosity contrast manifests a complex mixing dynamic of critical importance in various physics, such as thermohaline convection [2], inertial confinement fusion [3–5], liquid films [6], astrophysical flows [7,8], planetary mantle convection [9,10], extreme weather events [11], geophysical flows [12], ocean currents [13], and many more.

The RT instability in porous media (or equivalently in a Hele-Shaw cell) [14] has received significant attention and is generally characterized by the Rayleigh number, $\mathrm{Ra} = k\Delta\rho g H/\phi\mu D$, where k is the permeability, $\Delta\rho$ the maximum density difference, g the gravitational acceleration, H height, ϕ porosity, D the effective diffusion coefficient, and μ the fluid viscosity. The buoyancy-driven convection evolves when Ra exceeds a critical value (Ra_c) [15,16]. In the absence of viscosity contrast (i.e., fluid pairs with identical viscosities), the theory suggests a Ra_c of $4\pi^2$ [15,16]. However, when the mixture viscosity varies with the concentration, Ra_c is shown to be different [17,18].

In a gravitational field, the coupled effect of double diffusion and unfavorable density gradients may lead to convective instabilities [19]. These phenomena are particularly relevant in reactive and nonreactive multicomponent systems involving various solutes with different diffusion coefficients. Chemical reactions can influence or even initiate hydrodynamic instabilities by altering density, viscosity, and permeability profiles [20].

*hhassanz@ucalgary.ca

The evolution of Rayleigh-Taylor instability can generally be divided into several distinct regimes. Initially, a diffusive boundary layer forms due to the lighter fluid's diffusivity into the upper layer. This initial phase is called the diffusive regime, where the flux and mixing length scale with $\sqrt{t}$. As the diffusive boundary layer becomes denser over time, the system turns unstable and transitions into a convection-dominated regime where the mass flux is primarily driven by convection. Although mass transfer in this regime is mainly governed by convection, diffusion remains significant, leading to various mixing processes [21]. The convection-dominated vigorous mixing continues until the fingers contact the top or bottom boundary, marking the entry into the shutdown regime. During the shutdown period, the dissolution flux rapidly decreases with time, and diffusion once again becomes the dominant mechanism of mass transfer [22,23].

The effect of viscosity on the onset of buoyancy-driven flows has been widely studied [18,24,25]. However, the dynamics of RT mixing beyond the onset of instabilities at large viscosity ratios ($M > 3 \times 10^3$) has not been studied. Systems with large M and Ra are ubiquitous and often difficult to mimic experimentally in the lab or simulate numerically. Numerical simulations revealed that, in a gravitationally unstable flow, even though the symmetry of the up-down fingers across an interface is preserved up to $M_c \approx 20$, the viscosity contrast may delay the onset of nonlinear instabilities [12,19]. A maximum viscosity ratio of $M \approx 40$ was previously reported in experimental studies of RT instability [26]. In a recent simulation study for viscosity ratios up to $M \approx 3 \times 10^3$ [27], a critical mobility ratio of $M_c \approx 20$ was identified, beyond which a symmetry-breaking phenomenon is observed. Beyond the critical mobility ratio, the upward rate slows significantly while the downward rate remains unaffected. Mokrys and Butler [28–30] pioneered the study of the gravity drainage of an extremely viscous fluid by a solvent and observed the associated fingering. Nonetheless, their observation remained unexplained in the context of RT instabilities. In addition, there is currently a lack of a reduced order model that would allow for the prediction of the mixing interface location, interface velocity, and mass transfer across the interface at extreme viscosity ratios. Furthermore, a detailed experimental characterization of fingering asymmetry in RT instability at extreme viscosity ratios ($M > 3 \times 10^3$) has not been thoroughly explored in the past.

High-resolution numerical simulations of RT instabilities at large viscosity ratios ($M \sim 10^5$) and large Rayleigh numbers ($\mathrm{Ra} > 10^5$) are computationally expensive, if not impossible. In this work, we report RT mixing in a Hele-Shaw cell at a remarkably large viscosity ratio ($M \approx 5 \times 10^5$) and $\mathrm{Ra} \sim 10^5$–(3×10^6) and study the evolution of asymmetry in the growth of the fingers. We also develop a one-dimensional (1D) model to study RT mixing and quantify the mixing process by predicting the dissolution interface location, interface velocity, and mass transfer across the interface. The 1D reduced order model overcomes the demanding computational challenge and predicts the behavior of RT mixing at extreme viscosity ratios.

II. 1D MATHEMATICAL MODEL

Figure 1(a) shows the schematic of the problem studied. The origin is chosen at the upward-moving interface [$s(t)$]. We assume Boussinesq approximation and an isothermal system. Diffusion of the lighter fluid into the initially immobile heavy one mobilizes the latter. The mobilization of the heavy fluid leads to complex fingering instabilities where an upward dissolution moving front evolves.

We use the height of the cell (H), diffusion time (H^2/D), diffusion (D), and the interface concentration (c_i) to scale length, time, dispersion, and concentration, respectively. The dimensionless form of the cross-sectional average of the heavy fluid concentration (c) below the interface based on Taylor's assumptions is [31,32]

$$\frac{\partial c}{\partial t} = [1 + K(t)]\frac{\partial^2 c}{\partial z^2}, \tag{1}$$

where $c(z, t)$ is the horizontal cross-sectional average of heavy fluid concentration, and $K(t)$ is the dimensionless time-dependent mixing. The 1D horizontal cross-sectional average is considered

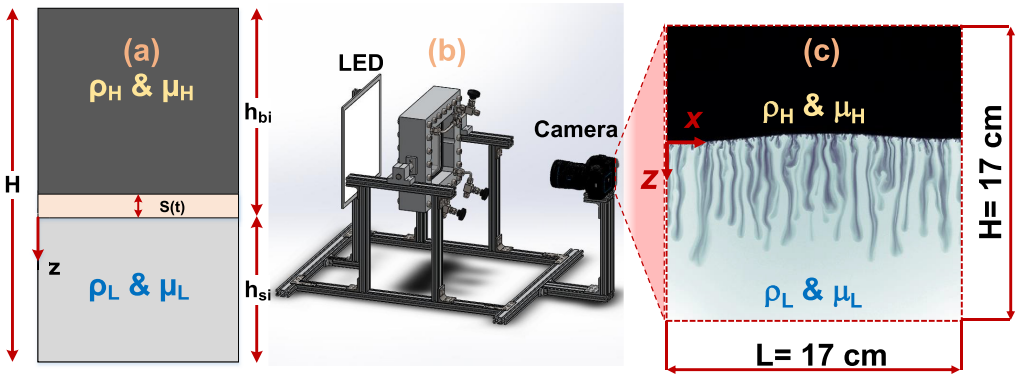

FIG. 1. (a) Schematic of the proposed model. h_{bi} and h_{si} are the initial height of heavy and light fluids in the cell, respectively. ρ_H and ρ_L are the density of heavy and light fluids, respectively, and μ_H and μ_L are the viscosity of heavy and light fluids, respectively. (b) The Hele-Shaw cell apparatus, along with the main parts of the setup, includes the camera, illumination system, and injection valves. (c) The domain of study captured during one of the experiments shows the flow evolution qualitatively for the present physical configuration. The reference frame (x, z), along with the height $(H = 17\,\text{cm})$ and length $(L = 17\,\text{cm})$ of the domain, are indicated.

to be sufficient based on our experimental observation of uniform concentration profiles at any vertical depth and previous theories on natural convection [31,33]. A time-dependent dispersion is considered based on the experimental observation of convective mixing in a closed system where vigorous mixing is followed by a shutdown period. The same approach has been previously used to model convective dissolution in the absence of viscosity contrast [31]. The initial concentration of heavy fluid below the interface is zero; thus the initial condition (IC) is $c(z, t = 0) = 0$. The domain below the interface can be considered semi-infinite at the early time, where it is bounded from the top by a moving interface. Hence, the boundary conditions (BCs) can be written as $c[z = s(t) \leqslant 0, t] = 1$ and $c(z \to +\infty, t) = 0$.

The following approach is applied to obtain the Stefan boundary condition [34] at the interface of heavy and light fluids. Equation (1) is integrated from $s(t)$ to $+\infty$:

$$\int_{s(t)}^{+\infty} \frac{\partial c}{\partial t} dz = (1 + K) \int_{s(t)}^{+\infty} \frac{\partial^2 c}{\partial z^2} dz. \tag{2}$$

By applying the Leibniz integration rule, we have

$$\frac{\partial}{\partial t}\left[\int_{s(t)}^{+\infty} c dz\right] + \frac{ds}{dt} = (1 + K) \int_{s(t)}^{+\infty} \frac{\partial^2 c}{\partial z^2} dz. \tag{3}$$

The right-hand side of Eq. (3) can be integrated as

$$\frac{\partial}{\partial t}\left[\int_{s(t)}^{+\infty} c dz\right] + \frac{ds}{dt} = (1 + K)\left[\frac{\partial c}{\partial z}\right]_{s(t)}^{+\infty} = -(1 + K)\left(\frac{\partial c}{\partial z}\right)_{z=s(t)}. \tag{4}$$

The mass of light fluid below the interface remains constant since the system is closed, and there is no mass loss. Hence

$$\int_{s(t)}^{+\infty} \rho A[1 - (cc_i)] dz = c_0, \tag{5}$$

where c_0 is a constant, $c_i = 0.5$ is the average mass fraction of heavy fluid at the interface, and A is the cross-sectional area of the Hele-Shaw cell ($A = Lb$; L is the cell width and b is the cell gap

thickness). Equation (5) can be further simplified as

$$\int_{s(t)}^{+\infty}\left(\frac{1}{c_i}-c\right)dz = c', \tag{6}$$

where $c' = c_0/\rho A$. Furthermore, Eq. (4) can be rewritten as

$$\frac{\partial}{\partial t}\left[-\int_{s(t)}^{+\infty}\left(\frac{1}{c_i}-c\right)dz+\frac{1}{c_i}\int_{s(t)}^{+\infty}dz\right]+\frac{ds}{dt} = -(1+K)\left(\frac{\partial c}{\partial z}\right)_{z=s(t)}. \tag{7}$$

Inserting Eq. (6) into Eq. (7), the final form of the upward-moving front of the heavy-light fluid interface equation will be

$$\frac{ds}{dt} = (1+K)\frac{c_i}{(1-c_i)}\left.\frac{\partial c}{\partial z}\right|_{z=s(t)}, \tag{8}$$

where the initial condition for the upward-moving front of the heavy-light fluid interface is $s(0) = 0$.

The heat integral method [34] is applied to Eqs. (1) and (8) using $c(z,t) = A_1z^3 + B_1z^2 + C_1z + D_1$ subject to the given IC and BCs to obtain the final form of the solutions. The IC, auxiliary, and main BCs can be written as

$$c[s(t) < z < \delta(t), t = 0] = 0, \tag{9}$$

$$c[z = s(t), t > 0] = 1, \tag{10}$$

$$c[z = \delta(t), t > 0] = 0, \tag{11}$$

$$\partial c/\partial z[z = \delta(t), t > 0] = 0, \tag{12}$$

$$\partial^2 c/\partial z^2[z = \delta(t), t > 0] = 0, \tag{13}$$

where $\delta(t)$ is the penetration depth of concentration [35]. Applying the IC and BCs results in $A_1 = (s-\delta)^{-3}$, $B_1 = -3\delta(s-\delta)^{-3}$, $C_1 = 3\delta^2(s-\delta)^{-3}$, and $D_1 = -\delta^3(s-\delta)^{-3}$. Therefore, the final form of the concentration profile is

$$c(z,t) = \left[\frac{z-\delta}{s-\delta}\right]^3. \tag{14}$$

Replacing $\partial c/\partial z|_{z=s(t)} = 3(z-\delta)^2(s-\delta)^{-3}$ into Eq. (8) results in

$$\frac{ds}{dt} = (1+K)\left(\frac{c_i}{1-c_i}\right)\left(\frac{3}{s-\delta}\right). \tag{15}$$

Penetration depth can be obtained by inserting c from Eq. (14) into Eq. (2) and applying the Leibniz rule from s to δ, giving

$$\frac{\partial}{\partial t}\int_s^\delta\left[\frac{z-\delta}{s-\delta}\right]^3 dz = (1+K)\int_s^\delta\frac{\partial}{\partial z}\left(\frac{\partial c}{\partial z}\right)dz. \tag{16}$$

The integration gives

$$\frac{\partial}{\partial t}\left[\frac{s-\delta}{4}\right] = (1+K)\left[\frac{3}{s-\delta}\right]. \tag{17}$$

Applying the chain rule to Eq. (17) results in

$$\frac{ds}{dt}-\frac{d\delta}{dt} = \frac{12(1+K)}{s-\delta}. \tag{18}$$

Substituting $\partial s/\partial t$ from Eq. (15) gives the penetration depth relation as

$$\frac{d\delta}{dt} = \frac{3(1+K)}{\delta - s}\left[4 - \frac{c_i}{1-c_i}\right], \tag{19}$$

where Eqs. (15) and (19) should be solved numerically using the Adam-Bashforth-Moulton methods [36].

The transient mixing $[K(t)]$ can be represented by a two-parameter Weibull function $[K = \beta(t/\theta)^{\beta-1}e^{-(t/\theta)^{\beta}}/\theta]$ [37], where $\beta > 0$ and $\theta > 0$ are the shape and scale parameters, respectively. A greater value of β signifies a more pronounced dispersion peak and a reduced mixing time. Conversely, when θ is larger, it indicates a diminished dispersion peak and an extended mixing duration. In other words, as β increases, the concentration of solute within the mixture is dispersed at a quicker rate, resulting in a shorter time required for thorough mixing. Conversely, a higher θ value signifies a slower dispersion, resulting in a less pronounced dispersion peak and a longer duration needed to achieve complete mixing. These parameters are determined using the experimental data through a Monte Carlo (MC) parameter estimation technique (see the Appendix).

The average concentration below the interface can be calculated by integrating the downward flux at the interface, $\partial\bar{c}(t)/\partial t = uc|_{z=s(t)} + (1+K)(\partial c/\partial z)_{z=s(t)}$, where $u = ds/dt$, $c|_{z=s(t)} = 1$, and $\partial c/\partial z|_{z=s(t)} = 3/(\delta - s)$; then $\bar{c}(t)$ is

$$\bar{c}(t) = |s(t)| + 3\int_o^t \frac{1+K}{\delta - s}dt. \tag{20}$$

The pure diffusion rate can be calculated as $q_{\text{diff}} = -\partial c/\partial z|_{z=s} = \exp(s^2/4t)/[\sqrt{\pi t}\,\text{erfc}(\lambda)]$ where $s = 2|\lambda|\sqrt{t}$ is the corresponding interface location and λ is the root of the transcendental equation: $\sqrt{\pi}\lambda e^{\lambda^2}\text{erfc}(\lambda) + c_i/(1-c_i) = 0$ [38]. The Sherwood number ($\text{Sh} = q_{\text{conv}}/q_{\text{diff}}$), a measure of convective to diffusive mass flux, can be evaluated as $\text{Sh} = [u + 3(1+K)/(\delta - s)]\sqrt{\pi t}\,\text{erfc}(\lambda)\exp(s^2/4t)$. The model described here will be used later to simulate the RT experiments.

III. EXPERIMENTAL SETUP AND MATERIALS

Experiments were performed in a Hele-Shaw cell consisting of two borosilicate glass plates which enabled visualization of RT instabilities. Stainless steel shims, cut with a high-precision computer numerical control (CNC) machine at varying thicknesses ($0.0508 < b < 0.254$ mm), were used between glass plates to attain the desired permeability. The cell was then sealed with high-quality, impermeable rubber. The cell was illuminated from the backside by a dimmable system of several LED lamps. A CCD camera was used to capture the flow evolution at high resolution. The three-dimensional (3D) sketch of the apparatus with all included parts is shown in Fig. 1(b). The apparatus was placed on a vibration-free table and covered by a black tent to eliminate external errors.

A. Working fluids

Bitumen (highly viscous and heavy) and toluene (less viscous, light, and fully miscible with bitumen) were used in the experiments. Bitumen has a viscosity on the order of $\sim 3 \times 10^5$ mPa s at room conditions and is used to create a high viscosity contrast. This pair makes a perfect choice to create a high-viscosity ratio of $M \approx 5 \times 10^5$, $\Delta\rho = 142.78\,\text{kg m}^{-3}$, and $D = 7.5 \times 10^{-10}\,\text{m}^2\,\text{s}^{-1}$ [39]. The density of mixtures of toluene and bitumen at a temperature of 20 °C is measured using an Anton Paar densitometer (DMA 5001), and the results are depicted in Fig. 2(a). The viscosity of mixtures of toluene and bitumen at a temperature of 20 °C is measured using a Hydramotion viscometer (XL7-HT), and the results are depicted in Fig. 2(b).

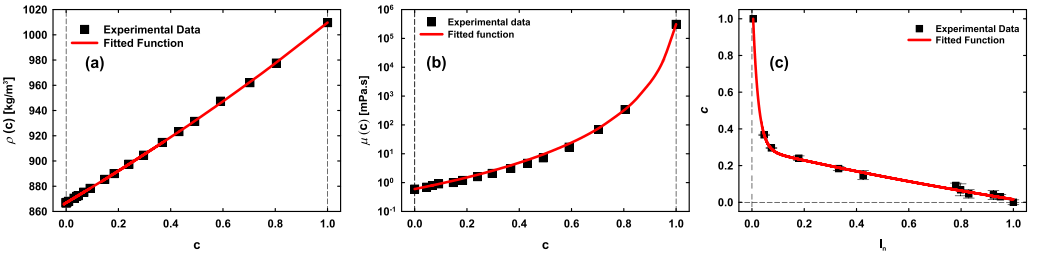

FIG. 2. (a) Density of mixtures of bitumen and toluene versus bitumen concentration (c). The experimental data (black squares) are fitted using the mixing rule (solid red line) $1/\rho_{\text{mix}} = c/\rho_H + (1-c)\rho_L$. Bitumen and toluene densities are $\rho_H = 1009.684$ and $\rho_L = 866.9 \pm 0.5\,\text{kg m}^{-3}$, respectively. (b) Viscosity of mixtures of bitumen and toluene versus bitumen concentration (c). The experimental data (black squares) are fitted properly using the power-law mixing rule (solid red line), $\mu(c) = \mu_L[c(e^{nR} - 1) + 1]^{1/n}$, where $n = -0.2275$. Bitumen and toluene viscosities are $\mu_H = 3.08 \times 10^5 \pm 10^4$ and $\mu_L = 0.6 \pm 0.02\,\text{mPa s}$, respectively. (c) Calibration curve for the gap thickness of $b = 0.0508\,\text{mm}$ at a given illumination condition against the normalized intensity $I_n (I_n = I/I_0)$. I_0 is the intensity of pure toluene. An exponential function, $c = a_0 + a_1 \exp(b_1 I_n) + a_2 \exp(b_2 I_n)$, (solid red line) could fit the experimental measurements (black squares with error bar).

B. Experimental procedure

Bitumen is immobile under room conditions. Hence, the Hele-Shaw cell was placed in an air bath oven, and the bitumen was injected at 80 °C using a Quizix pump at a rate of 0.05 ml/min to avoid any air bubbles trapping inside the cell until the fluid level has reached the middle of the cell. The cell was then left at room temperature for 24 h to cool down. The Hele-Shaw cell was subsequently placed on the vibration-free table. The illumination system and camera were set, and the whole setup was covered by the black tent. Toluene was injected gently from one side, and the air was pushed out from another side. The illumination system and camera were activated, and the experiment was started. The CCD camera (Canon EOS 1300D, 5184 × 3456 pixels, a lens with the specification of Canon EF-S 18–135mm f/3.5–5.6 IS STM) was set to capture images of the Hele-Shaw cell buoyancy-driven fingering every 5 s.

C. Image processing

The captured images represent the time-dependent two-dimensional (2D) concentration field of bitumen leached and drained into the toluene. The procedure of making a calibration curve that associates the light intensity with the bitumen concentration is described in the following section. The red channel of the RGB images, because it is brighter and has less noise, is utilized in the concentration field reconstruction process throughout this work.

D. Calibration

The construction of the calibration curve for different Hele-Shaw gaps and illumination conditions is a crucial step. Employing a single calibration curve for all cell gap values results in a significant error in the experimental flux calculations [40,41]. Therefore, several solution samples at various concentrations were utilized to construct the calibration curves, which enabled us to estimate the mixture concentration for each gap value. To do this, for a single gap, the cell was filled with a solution of a particular concentration and several pictures were captured for the sample. Then the mean intensity of the entire domain was obtained and reported as the final value. This procedure was repeated for the entire range of concentration. An example of the calibration curve for the gap thickness of $b = 0.0508\,\text{mm}$ is illustrated in Fig. 2(c). As shown, the normalized intensity does not vary significantly in the concentration range above 0.35, which could introduce errors in image processing and construction of the calibration curves.

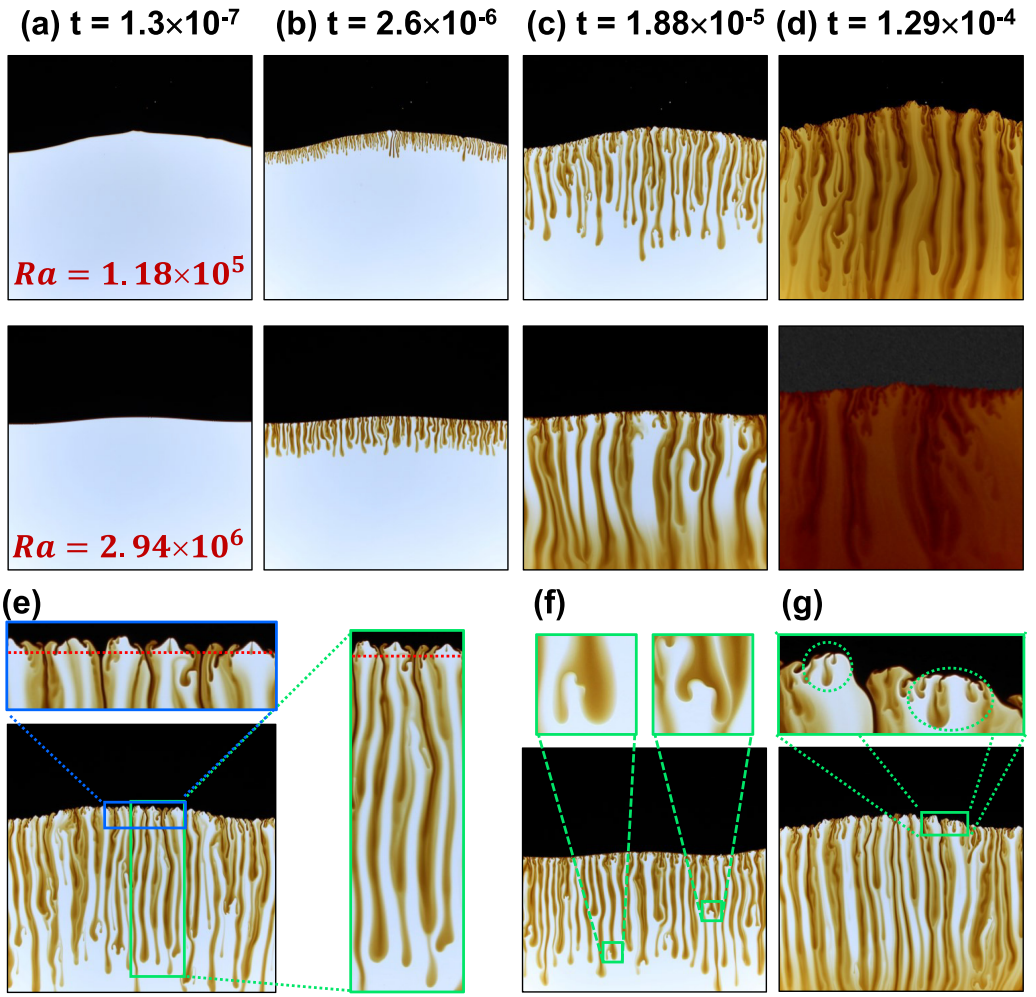

FIG. 3. [(a)–(d)] The snapshots of the experiments at different times for Ra $= 1.18 \times 10^5$ and Ra $= 2.94 \times 10^6$. Each row is for one Ra at different times. (e) Snapshot of asymmetrical growth of the fingers and high-wavelength upward fingers for Ra $= 4.7 \times 10^5$; the dashed red line shows the initial interface position. (f) Tip splitting of the downward fingers for Ra $= 1.44 \times 10^6$. (g) Mushroom-type baby fingers are observed within the upward fingers for Ra $= 4.7 \times 10^5$.

IV. RESULTS AND DISCUSSION

Figures 3(a)–3(d) show the experimental time evolution of the mixing process for Ra $= 1.18 \times 10^5$ and Ra $= 2.94 \times 10^6$. It was observed that, first, toluene diffuses into the bitumen through a short-lived diffusive regime, which leads to the formation of a diffusive boundary layer [Fig. 3(a)]. This layer, then, turns gravitationally unstable, leading to the evolution of bitumen-rich fingers penetrating downward [Fig. 3(b)]. As the mixing enters the dominant convective regime, the fingers continue moving downward and reach the bottom boundary, whereas the upward fingers have not yet formed [Figs. 3(c) and 3(d)]. An important observation was the asymmetrical growth of the upward and downward fingers where the fingers extend preferably downward [Fig. 3(e)]. This observation is in contrast with fingering behavior at low M, where a symmetric downward and upward fingering has been observed [42–44]. Moreover, the initial wavelength of the bitumen

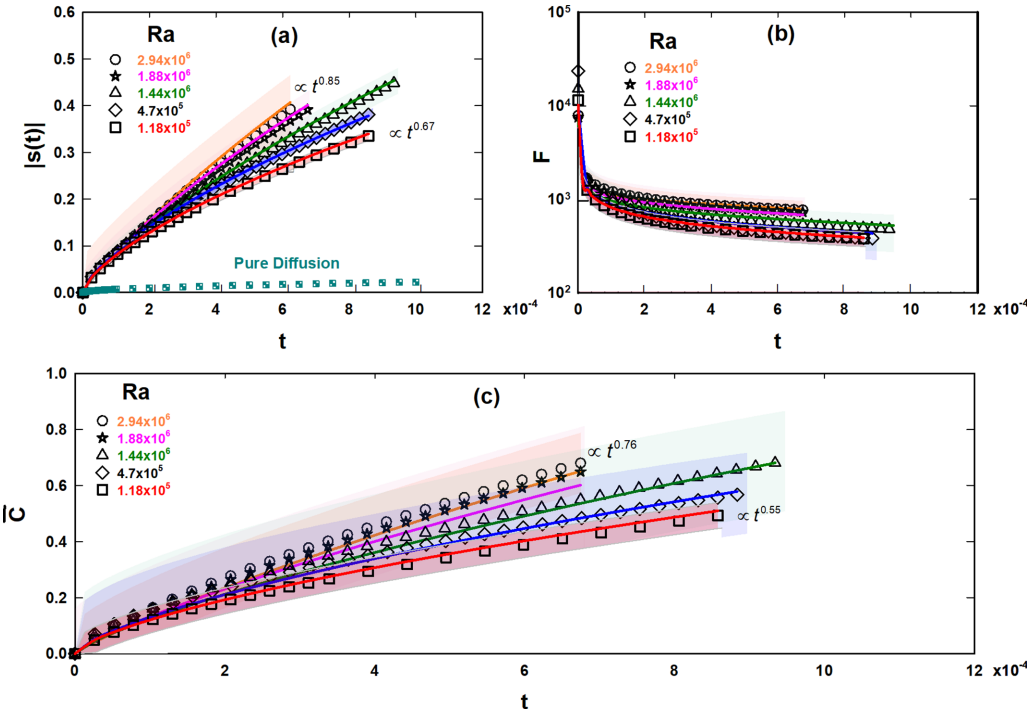

FIG. 4. (a) The interface location, (b) flux, and (c) average concentration of the dissolved bitumen in toluene below the interface, all versus time for different Ra [Ra $= (1.18 \times 10^5) - (2.94 \times 10^6)$]. The markers are the experimental data, and the lines show model prediction from Eqs. (15) and (20). The shadows indicate standard deviations from the experimental measurements.

fingers is very small [Fig. 3(b)]. However, due to the significant interaction of neighboring fingers and subsequent merging (see Movie S1 in the Supplemental Material [45]), the wavelength increases over time [Figs. 3(a)–3(c)]. It was observed that the bulk of bitumen remains immobile, and the mass transfer occurs solely at the interface through the leaching of viscous bitumen by toluene. It was also observed that the fingering remains downward for a significant period, and high-wavelength upward fingers are observed once the downward fingers touch the bottom boundary [Fig. 3(d)]. Furthermore, a significant tip splitting (Fig. 3(f); see Movie S2 in the Supplemental Material [45]) was observed where downward fingers of bitumen-rich fluid cleaved into multiple fingers. An interesting observation was the growth of an unstable boundary layer at the leading edge of the upward fingers, which eventually led to the formation of mushroom-type baby fingers (see Fig. 3(g) and Movie S3 in the Supplemental Material [45]). Ultimately, these small secondary fingers spread laterally and merged with the larger descending fingers. The upward growth of fingers persists during convective dissolution, ultimately reaching the upper boundary upon the arrival of the leaching interface. Upon reaching this stage, the process transitions to the shutdown regime with diminishing convection. A complete demonstration of one experiment conducted at Ra $= 4.7 \times 10^5$ is presented in Movie S4 of the Supplemental Material [45]. The nearly uniform concentration in a horizontal plane shown in Movie S4 confirms that a 1D reduced order model is sufficient to simulate the RT mixing.

The measured interface height, flux, and average concentration of the dissolved bitumen in toluene below the interface versus time for various Ra numbers are shown in Figs. 4(a)–4(c), respectively, and the results are compared with predictions obtained from the 1D model [Eqs. (15) and (20)]. The interface height, flux, and average concentration of the heavy fluid below the interface

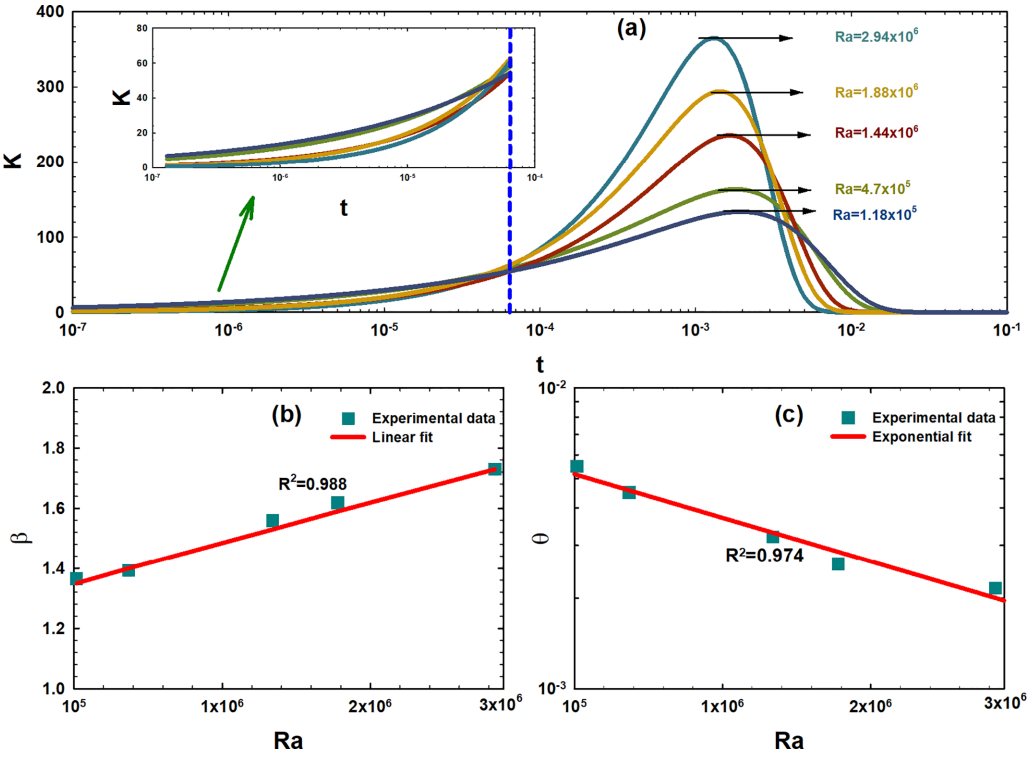

FIG. 5. (a) The dispersion coefficient versus time obtained using the experimental data through the MC approach; the inset plot shows the period before the fingers reach the bottom boundary. The dispersion parameters against Ra [$\mathrm{Ra} = (1.18 \times 10^5) - (2.94 \times 10^6)$]. (b) the shape parameter (β) and (c) the scale parameter (θ).

were obtained using image processing. The measured interface height [Fig. 4(a)] is compared with the pure diffusion case [38]. It is inferred that the interface velocity is significantly faster during the RT mixing ($t^{0.67–0.85}$) compared to the pure diffusion case ($t^{0.5}$). The model parameters (β and θ) are estimated using the experimental data through an MC parameter estimation approach (see the Appendix). The shaded area around the curves indicates standard deviations from the experimental measurements. As shown, the interface moved upward faster at higher Ra. As the system transitions to a convection regime, the mixing process is influenced by the formation of small fingers, which are then merged with neighboring fingers, resulting in a period of nearly constant flux [Fig. 4(b)]. At larger Ra numbers, the model predictions slightly deviate from the experiments. This deviation is due to the opaque nature of the toluene-bitumen mixture at high bitumen concentrations [Fig. 3(f)]. The calibration curve for each Hele-Shaw gap thickness is employed to reconstruct the concentration field. However, the image processing of the fingering patterns remained challenging due to their opaque nature. Therefore, the deviation between the experiments and the model is attributed to calibration accuracy.

A two-parameter Weibull function was found sufficient to represent the behavior of transient dispersion. The experimental data used in parameter estimation include the time evolution of the interface location and the average concentration of bitumen below the interface recorded during the experiments. A total realization of $N = 10^6$ was used to estimate the dispersion parameters and was found adequate when compared with $N = 10^4$ and $N = 10^5$.

Figure 5 shows the dispersion coefficient versus time obtained using the MC parameter estimation. As seen, the dispersion increases with Ra and grows over time until it reaches its maximum,

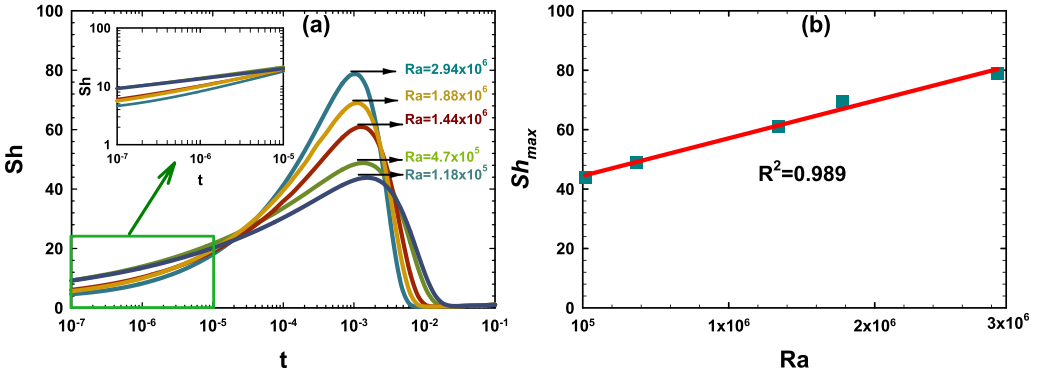

FIG. 6. (a) Sherwood number versus time at different Ra numbers [Ra $= (1.18 \times 10^5) - (2.94 \times 10^6)$], and (b) maximum Sherwood number versus Ra.

after which it rapidly declines. This behavior mimics the evolution of convective dissolution during the experiment, where mixing accelerates until the leaching interface arrives at the top of the cell. This is followed by a shutdown period, where the convective dissolution diminishes gradually. The inset plot in Fig. 5(a) highlights the dispersion behavior for different Ra numbers before the downward fingers reach the bottom boundary. The system shows higher dispersion at lower Ra numbers during the early stages before the fingers reach the bottom. This observation is because the fingers take longer to reach the bottom at lower Ra, resulting in a stronger convective mixing than higher Ra cases. However, this dynamic is short lived and not persistent, and once the fingers reach the bottom, a system with higher Ra leads to more vigorous mixing. In Fig. 5(a), a vertical dashed line indicates the time ($t \sim 6.4 \times 10^{-5}$) at which the fingers had already reached the bottom for all cases. The peaks in the dispersion curves indicate the time the upward-moving fingers reach the top. This is followed by a shutdown period and a subsequent decline in the dispersion coefficient. Figures 5(b) and 5(c) show the dispersion shape (β) and scale (θ) parameters versus Ra. A higher β suggests a higher dispersion peak but a shorter mixing time. In contrast, a larger θ indicates a lower dispersion peak and a prolonged mixing time. The shape parameter greater than 1 confirms the ascent and descent of convective mixing or the bell-shaped nature of the dispersion. The shape parameter increases linearly with Ra, implying more vigorous mixing at higher Ra. The scale parameter is an exponentially decreasing function of Ra, indicating a slower and prolonged mixing period at lower Ra.

The transient Sherwood number is shown in Fig. 6(a), which demonstrates a time-dependent evolution characterized by an initial increase, followed by a peak and subsequent decline, ultimately leading to a diminishing state. The maximum Sherwood signifies the time at which the upward fingers hit the top boundary and the onset of the shutdown period, during which the convective mixing gradually fades away. As expected, the Sherwood follows the same trend as the dispersion coefficient. The results indicate that the maximum Sherwood [Fig. 6(b)] increases linearly, suggesting more vigorous mixing at higher Ra. The inset plot in Fig. 6(a) illustrates the period before the downward fingers reach the bottom, during which the Sherwood is observed to be higher at lower Ra. This is because, at higher Ra, fingers reach the bottom faster than at lower Ra. Nevertheless, this dynamic is evanescent since the subsequent dynamic is dominated by the internal mixing for all Rayleigh numbers.

V. CONCLUSIONS

In closing, the maximum viscosity ratios reported in previous experimental and numerical simulation studies of RT instability have been $M \approx 40$ and $M \approx 3000$, respectively. In this work,

we reported RT mixing experiments and reduced order modeling with a large viscosity ratio ($M \approx 5 \times 10^5$) and high Rayleigh numbers (Ra $\sim 10^5$–3×10^6). The interface location between the two fluids and the average concentration below the interface were obtained from the high-resolution images. The experimental observations confirmed the fingering asymmetry phenomenon. Our findings reveal a short-lived diffusion period followed by a vigorous and nearly one-sided convective mixing when an extremely viscous fluid was placed above a less viscous and lighter fluid. High-wavelength upward fingers are observed when the downward fingers have already reached the bottom boundary. The downward fingers were found to grow vigorously and noticeably asymmetrically due to the large viscosity contrast between the two fluids during the dominant convective mixing. Furthermore, a significant merging of small fingers at the early period of the convection regime and tip splitting of the descending fingers are observed. The growth of secondary mushroom-type baby fingers at the leaching interface is confirmed. These secondary fingers eventually extend and merge with the larger descending fingers. The convection eventually enters a shutdown period when the leaching interface reaches the upper boundary. A 1D moving boundary problem with time-dependent dispersion is proposed to model the interface location and the overall mass transfer across the interface. The transient dispersion parameters are obtained using experimental data of interface location and overall mixing through an MC parameter estimation approach and are characterized using Ra. The results for all Ra reveal that the dispersion coefficient and Sherwood number follow a bell-shaped behavior where they grow with time, reach a peak, and decline rapidly.

ACKNOWLEDGMENTS

The authors acknowledge the financial support of Natural Sciences and Engineering Research Council of Canada (NSERC) and all the member companies of the SHARP Research Consortium.

APPENDIX: MONTE CARLO TECHNIQUE

The Monte Carlo simulation technique has been successfully used in several nonlinear and complex problems as a tool for parameter estimation [46]. Thus we used this technique to obtain the parameter values β and θ. The procedure of this technique is shown below.

(1) Set the number of realization or Monte Carlo sampling (N).

(2) Perform a random sampling for each parameter and generate input parameters for realization i using $\beta_i = \beta_{\min} + (\beta_{\max} - \beta_{\min})\zeta_i$ and $\theta_i = \theta_{\min} + (\theta_{\max} - \theta_{\min})\zeta_i$, where $\zeta_i \in [0, 1]$ is a random number.

(3) Obtain the dimensionless dispersion (K), using $K = \beta(t/\theta)^{\beta-1}e^{-(t/\theta)^\beta}/\theta$.

(4) Solve Eqs. (15) and (19) simultaneously to obtain s and δ.

(5) Obtain the average concentration ($\bar{c}$) using Eq. (20).

(6) Evaluate the objective function for realization i using $\varepsilon_i = \sum_{k=1}^{n}(|s_k^{\text{expt}} - s_k^m|/s_k^{\text{expt}} + |\bar{c}_k^{\text{expt}} - \bar{c}_k^m|/\bar{c}_k^{\text{expt}})$, where n is the number of time events; subscripts expt and m denote the experimental and model values, respectively.

(7) Repeat steps 2–6 for the specified number of realizations, N.

(8) Select a realization that results in minimum error ε_i and record the associated parameters, β_i and θ_i.

[1] R. A. Wooding, Growth of fingers at an unstable diffusing interface in a porous medium or Hele-Shaw cell, J. Fluid Mech. **39**, 477 (1969).

[2] Y. Ma and W. R. Peltier, Thermohaline-turbulence instability and thermohaline staircase formation in the polar oceans, Phys. Rev. Fluids **7**, 083801 (2022).

[3] J. P. Sauppe, S. Palaniyappan, B. J. Tobias, J. L. Kline, K. A. Flippo, O. L. Landen, D. Shvarts, S. H. Batha, P. A. Bradley, E. N. Loomis *et al.*, Demonstration of scale-invariant Rayleigh-Taylor instability growth in laser-driven cylindrical implosion experiments, Phys. Rev. Lett. **124**, 185003 (2020).
[4] S. I. Abarzhi and W. A. Goddard, Interfaces and mixing: Nonequilibrium transport across the scales, Proc. Natl. Acad. Sci. USA **116**, 18171 (2019).
[5] S. I. Abarzhi and K. R. Sreenivasan, Self-similar Rayleigh–Taylor mixing with accelerations varying in time and space, Proc. Natl. Acad. Sci. USA **119**, e2118589119 (2022).
[6] E. Jambon-Puillet, P. G. Ledda, F. Gallaire, and P.-T. Brun, Drops on the underside of a slightly inclined wet substrate move too fast to grow, Phys. Rev. Lett. **127**, 044503 (2021).
[7] D. E. Ruiz, D. A. Yager-Elorriaga, K. J. Peterson, D. B. Sinars, M. R. Weis, D. G. Schroen, K. Tomlinson, J. R. Fein, and K. Beckwith, Harmonic generation and inverse cascade in the *Z*-pinch driven, preseeded multimode, magneto-Rayleigh-Taylor instability, Phys. Rev. Lett. **128**, 255001 (2022).
[8] C. Liu, Y. Zhang, and Z. Xiao, A unified theoretical model for spatiotemporal development of Rayleigh–Taylor and Richtmyer–Meshkov fingers, J. Fluid Mech. **954**, A13 (2023).
[9] Y. Zhou, Rayleigh–Taylor and Richtmyer–Meshkov instability induced flow, turbulence, and mixing. II, Phys. Rep. **723–725**, 1 (2017).
[10] Y. Zhou, Rayleigh–Taylor and Richtmyer–Meshkov instability induced flow, turbulence, and mixing. I, Phys. Rep. **720–722**, 1 (2017).
[11] M. Franz and M. Zhang, Suppression and creation of chaos in a periodically forced Lorenz system, Phys. Rev. E **52**, 3558 (1995).
[12] A. J. A. Guzmán, M. Madonia, J. S. Cheng, R. Ostilla-Mónico, H. J. H. Clercx, and R. P. J. Kunnen, Competition between Ekman plumes and vortex condensates in rapidly rotating thermal convection, Phys. Rev. Lett. **125**, 214501 (2020).
[13] B. B. Cael and A. Mashayek, Log-skew-normality of ocean turbulence, Phys. Rev. Lett. **126**, 224502 (2021).
[14] O. Manickam and G. M. Homsy, Fingering instabilities in vertical miscible displacement flows in porous media, J. Fluid Mech. **288**, 75 (1995).
[15] C. W. Horton and F. T. Rogers, Convection currents in a porous medium, J. Appl. Phys. **16**, 367 (1945).
[16] E. R. Lapwood, Convection of a fluid in a porous medium, Math. Proc. Cambridge Philos. Soc. **44**, 508 (1948).
[17] M. R. Faradonbeh, T. G. Harding, J. Abedi, and H. Hassanzadeh, Stability analysis of coupled heat and mass transfer boundary layers during steam–solvent oil recovery process, Transp. Porous Media **108**, 595 (2015).
[18] N. Sabet, H. Hassanzadeh, and J. Abedi, A new insight into the stability of variable viscosity diffusive boundary layers in porous media under gravity field, AIChE J. **64**, 1083 (2018).
[19] S. S. Gopalakrishnan, J. Carballido-Landeira, B. Knaepen, and A. D. Wit, Control of Rayleigh-Taylor instability onset time and convective velocity by differential diffusion effects, Phys. Rev. E **98**, 011101(R) (2018).
[20] A. De Wit, Chemo-hydrodynamic patterns and instabilities, Annu. Rev. Fluid Mech. **52**, 531 (2019).
[21] S. S. Gopalakrishnan, J. Carballido-Landeira, A. D. Wit, and B. Knaepen, Relative role of convective and diffusive mixing in the miscible Rayleigh-Taylor instability in porous media, Phys. Rev. Fluids **2**, 012501(R) (2017).
[22] A. C. Slim, M. M. Bandi, J. C. Miller, and L. Mahadevan, Dissolution-driven convection in a Hele–Shaw cell, Phys. Fluids **25**, 024101 (2013).
[23] A. C. Slim, Solutal-convection regimes in a two-dimensional porous medium, J. Fluid Mech. **741**, 461 (2014).
[24] D. Daniel and A. Riaz, Effect of viscosity contrast on gravitationally unstable diffusive layers in porous media, Phys. Fluids **26**, 116601 (2014).
[25] N. Sabet, H. Hassanzadeh, and J. Abedi, Stability of gravitationally unstable double diffusive transient boundary layers with variable viscosity in porous media, AIChE J. **63**, 2471 (2017).
[26] S. Pramanik, T. K. Hota, and M. Mishra, Influence of viscosity contrast on buoyantly unstable miscible fluids in porous media, J. Fluid Mech. **780**, 388 (2015).

[27] N. Sabet, H. Hassanzadeh, A. D. Wit, and J. Abedi, Scalings of Rayleigh-Taylor instability at large viscosity contrasts in porous media, Phys. Rev. Lett. **126**, 094501 (2021).
[28] I. J. Mokrys and R. M. Butler, The rise of interfering solvent chambers: Solvent analog model of steam-assisted gravity drainage, J. Can. Pet. Technol. **32**, 26 (1993).
[29] R. M. Butler and I. J. Mokrys, Solvent analog model of steam-assisted gravity drainage, AOSTRA J. Res. **5**, 17 (1989).
[30] I. J. Mokrys, The rise of interfering solvent chambers: Solvent analog model of SAGD, Master's thesis, University of Calgary, 1989.
[31] H. E. Meybodi and H. Hassanzadeh, Mixing induced by buoyancy-driven flows in porous media, AIChE J. **59**, 1378 (2013).
[32] G. I. Taylor, Dispersion of soluble matter in solvent flowing slowly through a tube, Proc. R. Soc. London, Ser. A **219**, 186 (1953).
[33] H. E. Meybodi and H. Hassanzadeh, Hydrodynamic dispersion in steady buoyancy-driven geological flows, Water Resour. Res. **47**, W12504 (2011).
[34] M. N. Ozisik, *Heat Conduction* (John Wiley & Sons, Inc., New York, 1993).
[35] T. R. Goodman, The heat-balance integral and its application to problems involving a change of phase, J. Fluids Eng. **80**, 335 (1958).
[36] L. F. Shampine and M. W. Reichelt, The MATLAB ODE suite, SIAM J. Sci. Comput. **18**, 1 (1997).
[37] A. Kasnavi, J. W. Wang, M. Shahram, and J. Zejda, Analytical Modeling of Crosstalk Noise Waveforms Using Weibull Function, in *IEEE/ACM International Conference on Computer-Aided Design ICCAD 2004* (IEEE, New York, 2004), p. 141.
[38] N. Sabet, M. Khalifi, M. Zirrahi, H. Hassanzadeh, and J. Abedi, A new analytical model for estimation of the molecular diffusion coefficient of gaseous solvents in bitumen—effect of swelling, Fuel **231**, 342 (2018).
[39] H. Fadaei, J. M. Shaw, and D. Sinton, Bitumen-toluene mutual diffusion coefficients using microfluidics, Energy Fuels **27**, 2042 (2013).
[40] M. Alipour, M. D. Paoli, and A. Soldati, Concentration-based velocity reconstruction in convective Hele–Shaw flows, Exp. Fluids **61**, 195 (2020).
[41] M. Alipour and M. D. Paoli, Convective dissolution in porous media: Experimental investigation in Hele-Shaw cell, Proc. Appl. Math. Mech. **19**, e201900236 (2019).
[42] M. D. Paoli, D. Perissutti, C. Marchioli, and A. Soldati, Experimental assessment of mixing layer scaling laws in Rayleigh-Taylor instability, Phys. Rev. Fluids **7**, 093503 (2022).
[43] M. D. Paoli, F. Zonta, and A. Soldati, Rayleigh-Taylor convective dissolution in confined porous media, Phys. Rev. Fluids **4**, 023502 (2019).
[44] P. M. J. Trevelyan, C. Almarcha, and A. D. Wit, Buoyancy-driven instabilities of miscible two-layer stratifications in porous media and Hele-Shaw cells, J. Fluid Mech **670**, 38 (2011).
[45] See Supplemental Material at http://link.aps.org/supplemental/10.1103/PhysRevFluids.8.103504 for "Movie S1," time-dependant evolution of small fingers and subsequent merging for $\mathrm{Ra} = 1.88 \times 10^6$; "Movie S2," time-dependant evolution of tip splitting fingers for $\mathrm{Ra} = 1.88 \times 10^6$; "Movie S3," the formation of mushroom-type baby fingers and subsequent merging with larger descending fingers for $\mathrm{Ra} = 1.88 \times 10^6$; and "Movie S4," a full experiment at $\mathrm{Ra} = 4.7 \times 10^5$.
[46] M. Aggarwal and J. Carrayrou, Parameter estimation for reactive transport by a Monte-Carlo approach, AIChE J. **52**, 2281 (2006).